Editors' Suggestion

X-ray free electron laser tuning for variable-gap undulators

Heung-Sik Kang[1,*] and Henrik Loos[2]
[1]Pohang Accelerator Laboratory, Pohang, Gyeongbuk 37673, Republic of Korea
[2]SLAC, Menlo Park, California, USA

(Received 28 March 2019; published 21 June 2019)

A tuning method for hard x-ray free electron lasers is presented which combines electron-beam-based alignment (EBBA) with undulator radiation spectrum analysis. This method is conducive to achieving a dispersion-free orbit, finding the undulator field center, and determining the accurate value of the gap distance for the operating undulator K for each undulator segment, and it proves to be highly reliable and robust for free electron laser lasing with variable-gap undulators. The effect of the natural focusing of the undulator on the EBBA is confirmed with measurements and a theoretical analysis. The tilt of an undulator segment subject to ground movement introduces an undulator field change which the electron beam interacts with and can be corrected by K tuning to find a precise compensating gap distance. Lattice matching with a wire-scanner-based Twiss parameter measurement along the undulator line enables the EBBA reference orbit to coincide with the e-beam distribution.

DOI: 10.1103/PhysRevAccelBeams.22.060703

I. INTRODUCTION

For optimal operation of a hard x-ray free electron laser (XFEL), a stable electron beam in terms of energy, time, and orbit is required, and lower jitter is favorable for higher performance of the FEL and better time resolution for pump-probe experiments. Efficient self-amplified spontaneous emission (SASE) operation of a hard XFEL requires the orbit to be straight to within a few micrometers along the undulator line, which is achievable only by performing beam-based alignment (BBA). The requirements for lasing of a hard XFEL are very stringent (undulator K tolerance $\frac{\Delta K}{K} < 1.7 \times 10^{-4}$ and quadrupole position tolerance 1.2 μm for a 0.1 nm FEL [1]); therefore, lasing at wavelengths shorter than 0.1 nm is more difficult to achieve [2]. There are three notable factors that contribute to achieving lasing at hard XFELs. First, spatial overlap between the electron beam and the photon beam should be maximized along the typically 100-m-long undulator line. Second, spectral overlap of the undulator radiation from all undulators should be maximized. Third, the small emittance of the electron beam from the injector should be maintained along the accelerator and beam transport lines preceding the undulator line.

BBA for the undulator line is the first step in maximizing the spatial overlap between the electron beam and photon beam. Dispersion-free orbits straight to within a few micrometers over the gain length are possible only by BBA. Lattice matching for the undulator line is also crucial in achieving a uniform e-beam size along the undulator FODO lattice that is best overlapped with the photon beam. Small emittance is also important in effectuating the best overlap between them. Overlap in terms of the radiation spectrum between the electron beam and photon beam should also be maximized. Accurate undulator gap distance measurements as determined by K tuning are used to ensure the same wavelength radiation from all variable-gap undulators, and an undulator midplane height scan is employed to accurately control the undulator field center.

Two kinds of BBA for FEL undulator lines are currently used for XFELs: electron BBA (EBBA) [3,4] and photon BBA (PBBA) [5]. Even though each scheme is sufficient to realize FEL lasing when used independently, a combination of the two schemes may enable more robust FEL lasing than either scheme alone. The EBBA method developed at linac coherent light source (LCLS) [6] is based on a fixed-gap undulator line, while variable-gap undulators are being or will be used in most hard XFELs, such as the PAL-XFEL [4], Spring-8 Angstrom Compact Free Electron Laser [7], SwissFEL [8], European XFEL [9], and LCLS-II [10]. EBBA is relatively easy to implement, because it uses well-defined accelerator optics. However, it was found at the PAL-XFEL that if only EBBA is used for variable-gap undulators, poor alignment along the undulators and lasing failure may result due to uncertainties in the undulator gap distance and field center, which cannot be compensated for

*hskang@postech.ac.kr

in EBBA. When a new reference electron beam orbit is established by performing EBBA, the undulators should be offset vertically with respect to it, because offset corrections of EBBA are applied only to the quadrupoles and beam position monitors (BPMs), while the vertical positions of the undulators are left at their initial values. Therefore, the radiation spectrum analysis used in PBBA is necessary to find the field center of each undulator. The tuning method combining the two schemes is very reliable and robust, characteristics that are particularly essential for variable-gap undulators. The sequence of this method is as follows: EBBA, undulator midplane height scan, and undulator K tuning.

The PAL-XFEL consists of a 10 GeV S-band normal conducting linac delivering an electron bunch to two undulator lines [a hard x-ray undulator line (HX1) and a soft x-ray undulator line (SX1)] [11]. The hard XFEL line contains five acceleration sections (L0, L1, L2, L3, and L4), three magnetic bunch compressor chicanes (BC1, BC2, and BC3H), and an achromatic dogleg transport line with a bend angle of 0.5° to the hard x-ray undulators (see Fig. 1). L0 represents a 135 MeV injector consisting of the PAL-design photocathode rf gun and two S-band J-type accelerating structures. A laser heater system consisting of a 50-cm-long undulator and four dipoles is to mitigate microbunching instability. An X-band cavity for linearization, which is 75 cm long, is placed right after L1. The design beam energies are 0.33 GeV at BC1, 2.5 GeV at BC2, and 3.4 GeV at BC3H. Twenty undulator segments were installed in HX1, and seven segments were installed in SX1. We adopted the European XFEL undulator design [12], such as a 5-m-long, planar, permanent magnet and an out-vacuum variable-gap undulator, and modified our magnet design according to the PAL-XFEL undulator parameters. Figure 2 shows the lattice function of the PAL-XFEL. Beta functions are smaller than 85 m throughout the line. The three-bunch-compressor scheme is useful in allowing a small bend angle (1.6°) in the last chicane dipole, which can help reduce emittance growth as well as transverse kicks due to strong coherent synchrotron radiation.

II. ELECTRON-BEAM-BASED ALIGNMENT

The EBBA for the undulator line is based on a well-known accelerator lattice, and its purpose is to find the correct offsets of the BPMs and quadrupoles to achieve a dispersion-free orbit. The details of the EBBA algorithm can be found in the Appendix. The lattice of the undulator line is typically a FODO type in an array of one quadrupole and a drift between quadrupoles where one undulator is placed (see Fig. 3). For the PAL-XFEL, the interspace between undulators is 1.05 m long for both HX1 and SX1 and is occupied with a quadrupole, a BPM, and a phase shifter controlled by individual movers. The quadrupole is a combined function type with horizontal and vertical correctors incorporated. In the EBBA, the electron beam positions are measured with BPMs at four different beam energies to accurately measure and correct the dispersion along the undulator line: 4.0, 5.0, 6.67, and 10.0 GeV. Next, the offset values of BPMs and quadrupoles for a dispersion-free orbit are calculated. The calculated values are then applied to the BPM's BBA offset setting and the quadrupole mover offset. These two steps are repeated until all of the calculated BPM offsets become smaller than 5 μm. It takes about 10 min to finish one iteration, and at least seven or eight iterations are required to complete the process. The accuracy of EBBA strongly depends on the BPM reading accuracy so that a submicron resolution BPM like an X-band cavity BPM is used [13].

In HX1, we are using 24 cavity BPMs for 20 undulators (a self-seeding section is located right after the eighth undulator). We carried out the cavity BPM calibration with the cavity BPM mover. Each cavity BPM pickup is equipped with its own mover with the maximum moving distance of ± 1.5 mm for both horizontal and vertical directions. The measured BPM resolution is below 1 μm for all BPMs at a beam charge of 150 pC.

The EBBA for HX1 was done with the undulator gap closed down to 9.0 mm. The first iteration of EBBA resulted in rather high values of offsets up to 200 μm for both BPMs and quads, which became smaller as more BBA iterations were being taken, and after the eighth

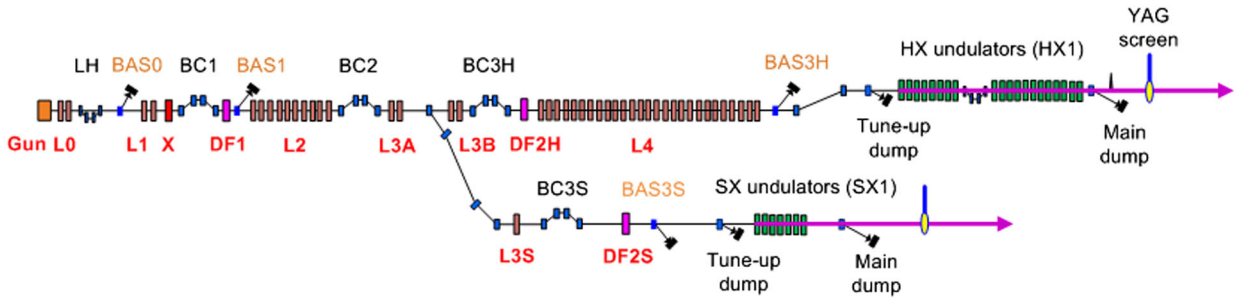

FIG. 1. Schematic diagram of the PAL-XFEL. L0 is the injector; L1, L2, L3A, L3B, L4, and L3S, acceleration sections; X is an X-band linearizer cavity; DF1, DF2H, and DF2S, deflector cavities; LH is a laser heater; BC1, BC2, BC3H, and BC3S, magnetic bunch compressor chicanes, whose dipoles are rectangles in blue; BAS0, BAS1, BAS3H, and BAS3S, beam analysis stations, each of which consists of a dipole (rectangle in blue), a YAG screen, and a dump (rectangle in black).

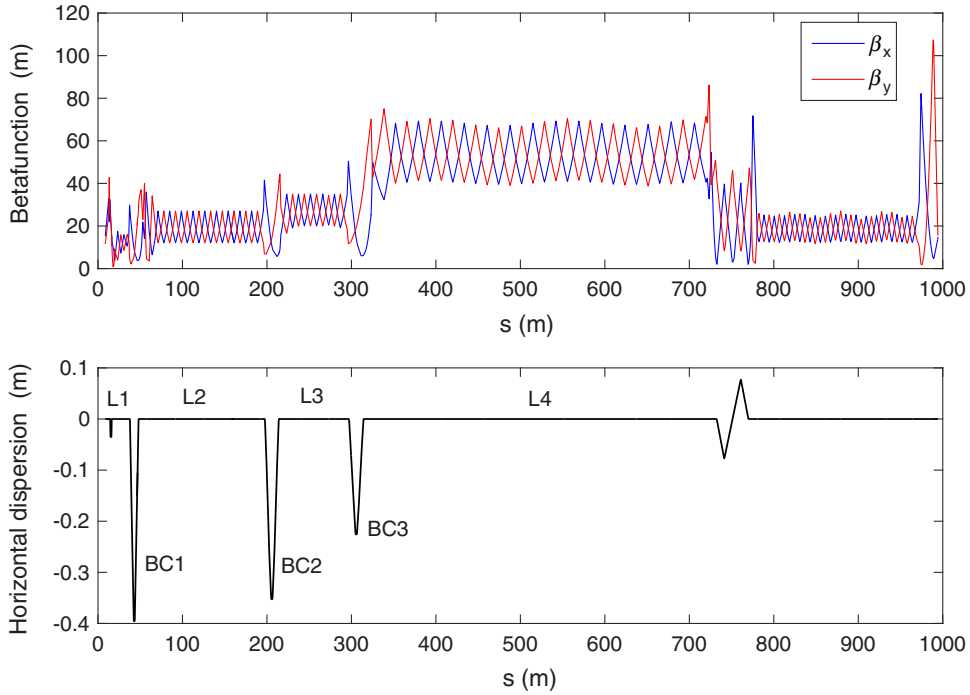

FIG. 2. Lattice function of the PAL-XFEL. The beta function and horizontal dispersion as a function of s from the end of the injector ($s = 8.6$ m) to the main dump ($s = 994$ m). The position of the gun cathode is $s = 0$.

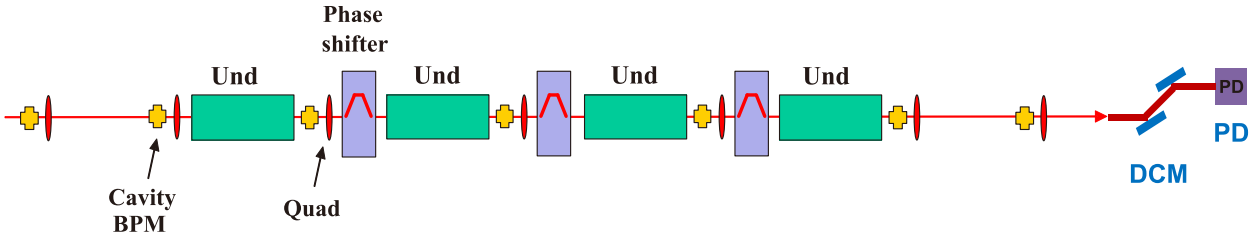

FIG. 3. Layout of the undulator line. A DCM and PD (photodiode) are located at the beam line optical hutch.

iteration shrank down to below 5 μm for all BPM offsets (see Fig. 4). Figure 5 shows the change of a particular quadrupole's vertical offset as a function of the number of BBA iterations. It changed a lot after the first iteration of EBBA and subsequently shrank down to below 10 μm after the following iterations. In the soft x-ray undulator line, ten cavity BPMs are used for seven undulators with measurements taken at four different beam energies of 1.9, 2.2, 2.5, and 3.0 GeV for the EBBA.

During the initial PAL-XFEL commissioning, significant differences in the EBBA fit solution for both BPMs and quadrupoles between measurements with fully opened and closed undulator gaps were found in the vertical plane, indicating an artificial effect from the natural focusing of the undulators.

The exact undulator field for a planar undulator with flat poles is

$$\vec{B} = B_o \cosh(k_u y)\sin(k_u z)\hat{y} + B_o \sinh(k_u y)\cos(k_u z)\hat{z}. \quad (1)$$

The z component of the undulator field, which is the fringe field, introduces its natural focusing in the vertical plane as a kick: $\frac{d^2 y_\beta}{dz^2} = -(\frac{K_0^2 k_u^2}{2\gamma_0^2}) y_\beta$.

In order to evaluate the effect of undulator focusing on the EBBA, we carried out the EBBA with a known vertical offset for all undulators. To introduce sufficient strength of the undulator focusing, the undulator gap was closed to 9.0 mm. Initially, all of the undulators' field centers were placed at $y = 0$, established with EBBA, by using the undulator spectrum analysis (the undulator gap distance is adjustable from 8.6 to 200 mm, and the undulator midplane height is remotely adjustable by ± 200 μm), and then all undulators were offset by $+100$ and -100 μm in the vertical direction. The beam energies were chosen at 4.1, 5.1, 6.6, and 10.0 GeV.

Figure 6 clearly shows a bow pattern of BPM offsets and quad offsets in the vertical plane. The standard EBBA offset fits with fit constraints on the BPM offsets shown in Figs. 6(a) and 6(b) exhibit a 50 μm depth bow pattern in the

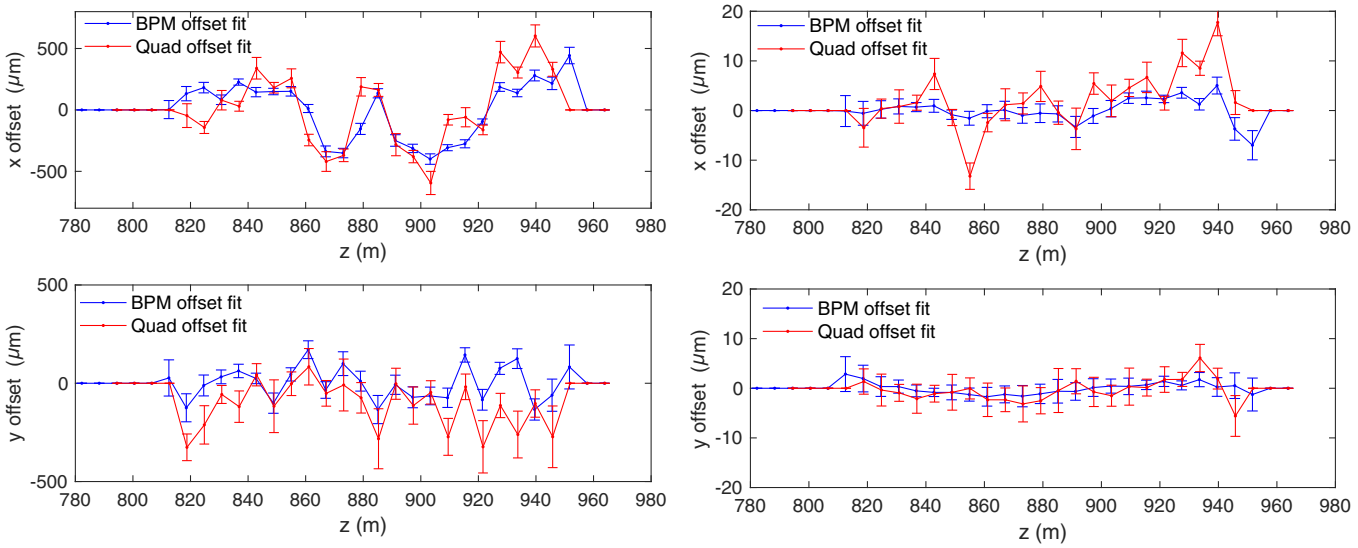

FIG. 4. (a) Displacements needed to correct the alignment of the BPMs and quadrupoles calculated by the EBBA algorithm for the hard x-ray undulator line are depicted with error bars representing the rms statistical uncertainties (red points and bars) and (b) after the last (eighth) iteration of the EBBA process. In (a), "X offset" and "y offset" represent horizontal and vertical displacements necessary to correct the alignment, respectively. In (a) and (b), 20 undulator segments are placed from $z = 820$ m to $z = 940$ m.

vertical plane, which is accumulated from approximately 0.13 μrad kick per undulator, while the X plane does not show any difference. In both planes, the uncertainty of the BPM offsets is about 2 μm, indicating a valid fit as this is close to the BPM resolution. If no fit constraints are applied, which allows for the BPM axis to float, the fits shown in Fig. 6(c) recover straight lines for the offsets which correspond almost exactly to the applied offsets for the undulators (with, e.g., the undulators raised, the BPM and quadrupole offsets are found too low by the same amount). The fit result moves the BPMs and quadrupoles to the undulator gap centers. Although this unconstrained fit is not sensitive to offsets in the undulator axis and does not generate an artificial bow pattern, the uncertainty in fitting

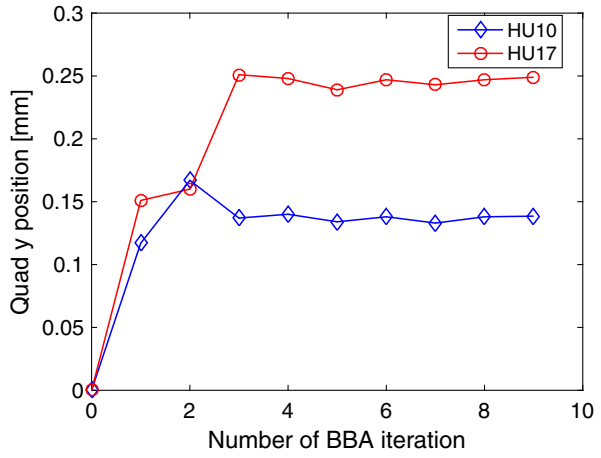

FIG. 5. Vertical offset of quadrupoles for undulators HU10 and HU17 as a function of the number of BBA iterations.

the BPM axis amplifies the error bars by an order of magnitude to about 20 μm and is as such not a viable method to accurately determine the individual BPM and quadrupole offsets. The bow pattern of the offsets found in the constraint fit are artifacts from offset undulators, and such fit solutions should not be implemented. To minimize this effect, the undulator offsets with respect to the electron beam axis should be adjusted to be close to zero or the undulator gaps be opened.

The artificial bow pattern in the EBBA solution for the constrained fit can be understood when considering the undulator natural focusing in the vertical plane. As detailed in the Appendix, the measured beam orbits at the different beam momenta are affected not only by the BPM and quadrupole offsets, but also by other magnetic fields not incorporated into the algorithm such as Earth's magnetic field, residual first and second field integrals remaining after undulator pole shimming, or other dipole fields from surrounding building or support structures. Their net effect on the beam within one undulator section between two adjacent quadrupoles can generally be expressed as a first and second field integral, and the EBBA algorithm will find appropriate offsets for the upstream and downstream quadrupole to exactly compensate the effect of these fields. This compensation works because the kick from a quadrupole offset by Δy_Q is $\Delta y' = \frac{e}{p}\frac{\partial B_x}{\partial y} L \Delta y_Q$ and can be expressed via a first field integral $I_{1x,Q}$ by $\Delta y' = \frac{e}{p} I_{1x,Q}$, since it scales with the inverse momentum p.

While the natural focusing of a centered undulator is incorporated into the EBBA algorithm through the undulator transfer matrices (see the Appendix), the effect from

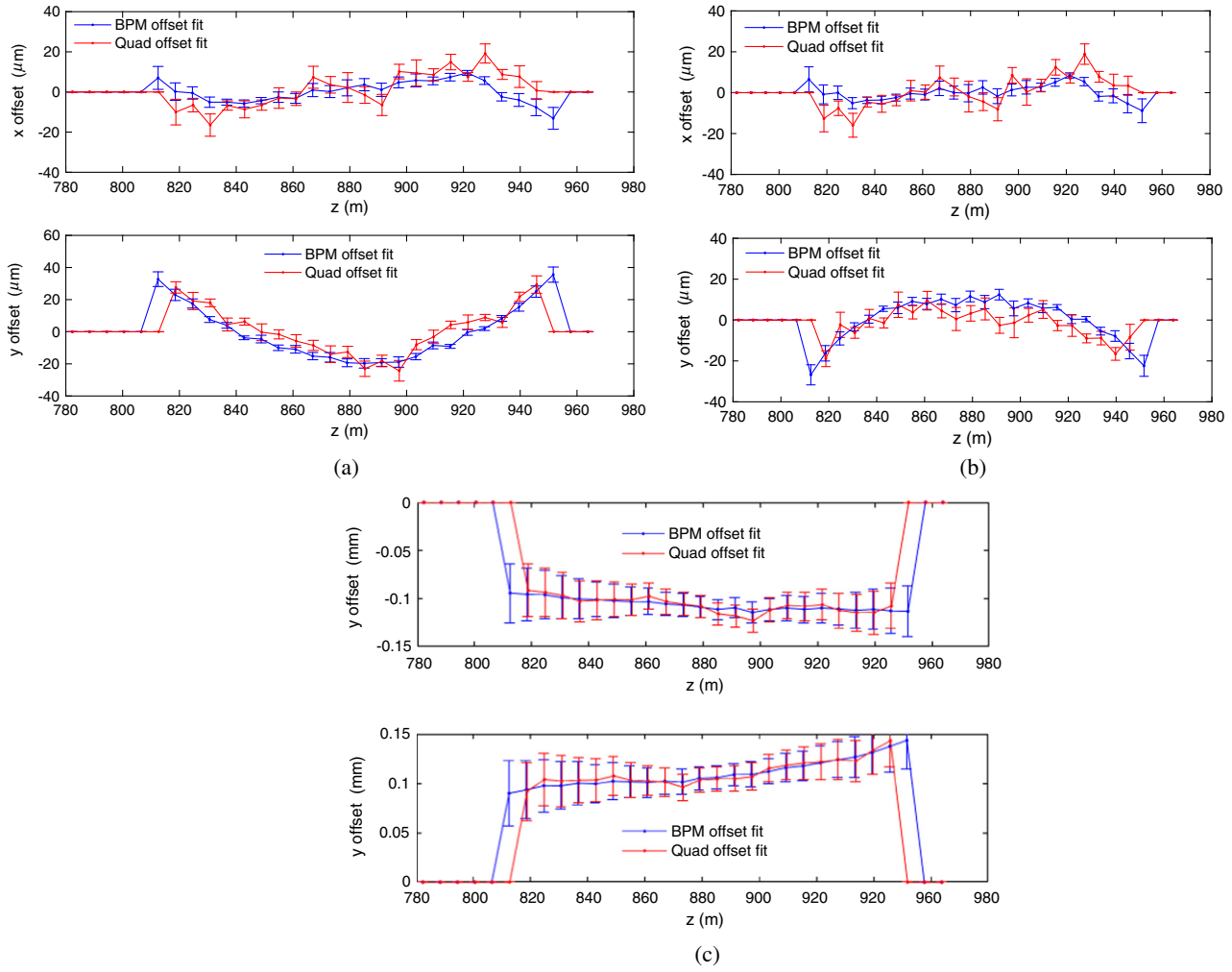

FIG. 6. (a) BPM and quad offsets in case of a $+100$ μm offset of the undulators, (b) BPM and quad offsets in the case of a -100 μm offset of the undulators, and (c) "floating" BPM axis fit of (a) (upper figure) and (b) (lower figure).

an off-axis undulator is not, and the resulting kicks also need to be compensated by quadrupole offsets as described above. The kick $\Delta y'$ from the natural focusing of an undulator offset by Δy_U, $\Delta y' = \frac{1}{\gamma^2}\frac{K^2}{2}k_U^2 L \Delta y_U$, can be written as $\Delta y' = \frac{e^2}{p^2} J_{1x,U}$ with $J_{1x,U}$ being a constant term. This kick scales with the inverse momentum squared and therefore cannot be expressed as a momentum-independent field integral.

Figure 7 depicts the vertical plane of a simplified undulator beam line configuration with only offset quadrupoles (Δy_{Qi}) and undulators (Δy_{Ui}) and no other field contributions or BPM offsets. It is further assumed as shown in the measurements in Fig. 6 that the same undulator offset between each quadrupole is applied. For an incoming beam angle y_1' upstream of the first quadrupole, the beam angle y_2' after passing through one quadrupole and one undulator at momentum p_n is then $y_2' = y_1' + \frac{e}{p_n} I_{1x,Q} + \frac{e^2}{p_n^2} J_{1x,U}$. An EBBA solution of this system of equations for the necessary quadrupole field integrals (and, hence, offsets) to obtain a straight and dispersion-free beam orbit would require that the incoming beam angle y_1' be maintained with $y_2' = y_1'$ throughout consecutive lattice cells. However, a solution for $I_{1x,Q}$ does not exist for the range of beam momenta p_n.

It is possible to construct a "bowed" solution if a constant deviation angle α is included for each lattice cell with $y_2' = y_1' + \alpha$. Then the system of equations becomes $\alpha = \frac{e}{p_n} I_{1x,Q} + \frac{e^2}{p_n^2} J_{1x,U}$ with an approximate best fit solution

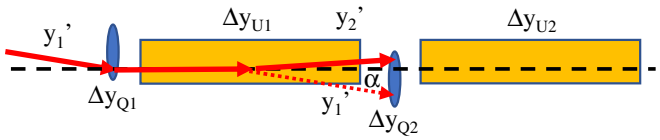

FIG. 7. Representation of kicks from quadrupole (Δy_{Qi}) and undulator (Δy_{Ui}) offsets. The incoming beam angle is y_1', and the beam angle after the first undulator is y_2'. The total change in the angle across one lattice cell is denoted by α.

for α and $I_{1x,Q}$ at given momenta p_n and undulator offset term $J_{1x,U}$. For only two energies, the exact solution is $\alpha = \frac{-e^2}{p_1 p_2} J_{1x,U} = \frac{-1}{\gamma_1 \gamma_2} \frac{K^2}{2} k_U^2 L \Delta y_U$. In the above PAL-XFEL case, $K = 1.87$, $\lambda_U = 2.6$ cm, $\Delta y_U = 100$ μm, and $L = 5.0$ m, the result for the bow angle α is 0.33 μrad if taking the lowest and highest energy vs 0.13 μrad from the EBBA result shown in Fig. 6(a). If these data are fitted using only the lowest and highest energy, the resulting bow corresponds to a kick angle of 0.27 μrad per undulator segment, signifying reasonable agreement between the fit to the data and the simple theoretical analysis for the bowed fit presented here. Simulations of the EBBA with offset undulators confirm the bowed solution and that, when implementing such a solution, the algorithm converges to an apparently straight and dispersion-free orbit which is based on actual quadrupole and BPM offsets that both follow the same curved trajectory. This can potentially result in a beam orbit deviation far beyond the orbit tolerance for SASE operation that would go unnoticed, since the beam orbit measurement would show a straight line.

In order to avoid this undulator focusing effect, it is best to perform the EBBA with fully opened undulator gaps, particularly for the initial commissioning of an undulator beam line.

III. UNDULATOR SPECTRUM ANALYSIS

The undulator spectrum analysis is used to precisely determine the undulator gap distance for each undulator to radiate at the same wavelength (called K tuning) and find the undulator field center of each undulator with respect to the reference orbit determined by EBBA. For 20 undulators at HX1, we are using a double crystal monochromator (DCM) with a resolution of 1×10^{-4} and a photodiode located at the beam line optical hutch (see Fig. 3). The electron beam needs to be uncompressed to have a relative energy spread smaller than the resolution of the DCM to optimize the resolution of the spectrum measurement. A slit, 6.7 mm wide and 6.7 mm high, is placed 192 m downstream of the first undulator (HU01), and the DCM is 3.5 m farther away from the slit.

A. K tuning

First, the undulator radiation spectrum from a specific undulator (normally, the first segment) is measured to determine the central photon energy, which is 7.0 keV in the case of an e-beam energy of 7.25 GeV and an undulator K of 1.87. Then, the DCM is set at the measured photon energy, and the undulator radiation spectrum of each undulator as a function of the undulator gap distance is measured. Figure 8(a) shows the photodiode current as a function of the undulator gap distance for 11 undulators out of 20. A large variation of the spectra for those undulators means that the gap distance of each undulator differs quite significantly to obtain the same undulator K. It is clearly seen that the upstream undulators like HU01 and HU02 show a rapid decrease of the photodiode current as the undulator gap increases, meaning that lower-energy photons with a large divergence are collimated by the slit, while the last undulator (HU20) shows a plateau at higher gap distances. To determine the undulator gap based on the measured data shown in Fig. 8(a), we used the fitting formula $f(g) = [a_1 + a_4(g - a_2)]\mathrm{erf}(-\frac{g-a_2}{a_3}) + a_5 + a_6 g$, where erf is the error function and g is the undulator gap; a_1, a_2, a_3, a_4, a_5, and a_6 are the fitting coefficients; and a_2 represents the determined gap distance [5]. The circle of the HU01 spectrum in Fig. 8(a) marks the gap distance determined by using the fitting formula.

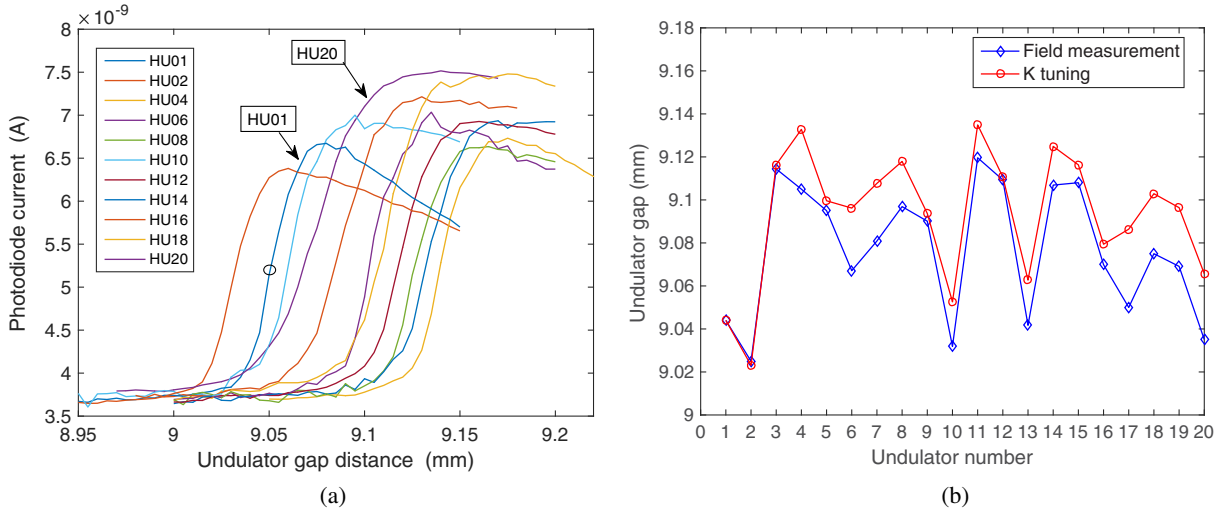

FIG. 8. (a) Undulator radiation spectrum of 11 undulators among 20 at HX1 and (b) undulator gap distances determined by both the field measurement and K tuning. The circle of the HU01 spectrum in (a) marks the gap distance determined by using the fitting formula in the main text.

K tuning is usually done after confirming the vertical offset of each undulator with respect to the reference orbit determined by EBBA. K tuning is a very accurate method to determine the gap distance of an undulator corresponding to a specific K with an accuracy of better than 2 μm. It turns out that the undulator gap distances determined by K tuning are different from the undulator field measurement [see Fig. 8(b)], meaning that the undulator field measured at the test bench is not same as the field measured by the e beam through undulator radiation. The worst case of the differences is as high as 30 μm, which corresponds to 5×10^{-3} of $\frac{\Delta K}{K}$. The gaps determined by the K tuning follow the trend of the field measurement, but the difference between both does not appear to be systematic, and the effect of longitudinal wakefields of the electron beam through the 6.4-mm gap undulator chamber is not clearly seen, because a relatively low peak current (~150 A with the beam charge of 180 pC) of electron beam is used in the measurement. Lasing can be consistently achieved only when the gaps of all 20 undulators are set at the gap distances determined by the K tuning (before the undulator tapering is applied). One of the reasons for the discrepancy between the field measurement and the K tuning is the tilt of undulator segments in the beam direction, which is described in the next section.

B. Undulator field center

The exact vertical position of the undulator field center is where the undulator field amplitude is minimum so that the intensity of undulator radiation passing the DCM should be highest at the center. The midplane height of each undulator is scanned to find the undulator field center with respect to the BBA reference orbit. It is possible to remotely adjust the undulator midplane height as much as ± 200 μm, which is enough to find the undulator field minimum. An electron beam with the same property for K tuning is used for this measurement. Figure 9(a) shows an example of the undulator field center measurement for HU13 at HX1 by using a DCM and a photodiode. The exact position of the undulator field center is around -0.08 mm in Fig. 9(a). An example of the measured undulator midplane offsets for 20 undulators is shown in Fig. 9(b). A typical pattern of the ground motion of the undulator hall is clearly shown in the figure: The upstream and downstream parts of the undulator hall are going up, while the middle part is going down.

C. Tilt of undulator segment

We observed that the gap distance determined by K tuning is changing over time (see Fig. 10). The main reason for this change is the tilt of the undulator segments in the beam direction with respect to the EBBA reference orbit as shown in Fig. 11. The EBBA reference orbit is established every two weeks while the vertical offsets of all the undulator segments are adjusted remotely according to the undulator field center measurement, which is subject to ground motion, mostly vertically, of the undulator hall floor. Since the ground motion is not uniform along the 200-m-long undulator hall, a tilt of the undulator segment in the beam direction is developing concurrently with the ground motion.

The purpose of the undulator field center measurements is to find the minimum of the field integral of an undulator segment that the electron beam traverses. As the tilt is increasing, the field integral amplitude is also growing. To compensate this, the undulator gap distance should be increased to maintain the same undulator K.

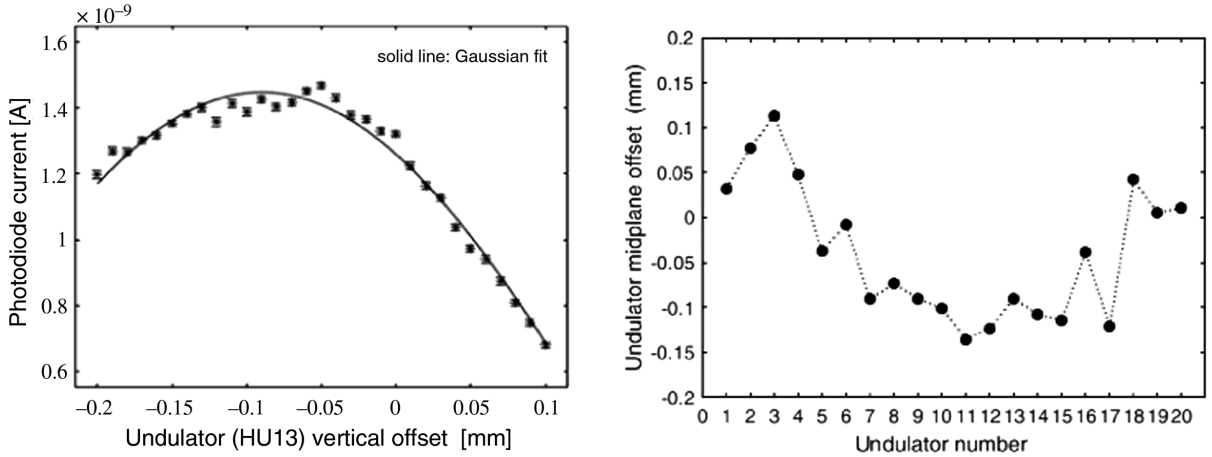

(a) (b)

FIG. 9. (a) Measurement of the undulator midplane for the undulator HU13 of HX1 and (b) an example of the measured undulator midplane offsets for 20 undulators. In (a), the photodiode current after a DCM is depicted as a function of the vertical offset. The undulator field center where the undulator field amplitude is minimum is around -0.08 mm.

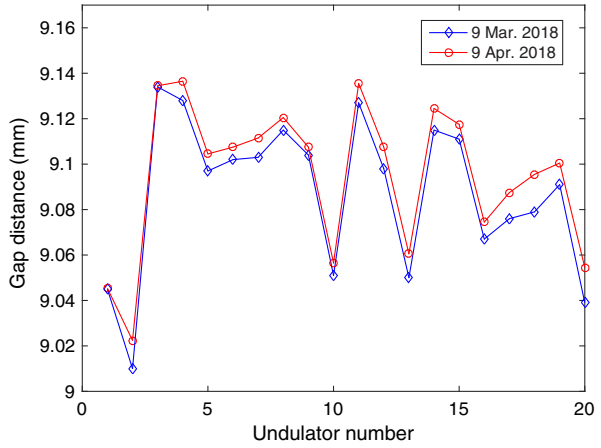

FIG. 10. Undulator gap distances determined by K tuning on 9 March 2018 and one month later. The alignment work for magnets and undulators is done twice a year (in February and July).

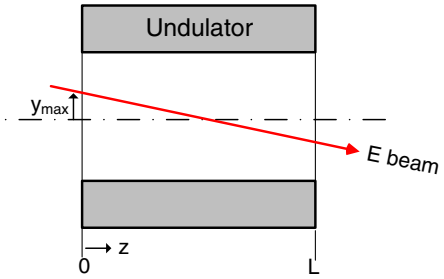

FIG. 11. Tilt of the undulator segment in the beam direction with respect to the EBBA reference orbit represented by the e-beam path. L is the undulator length (5 m).

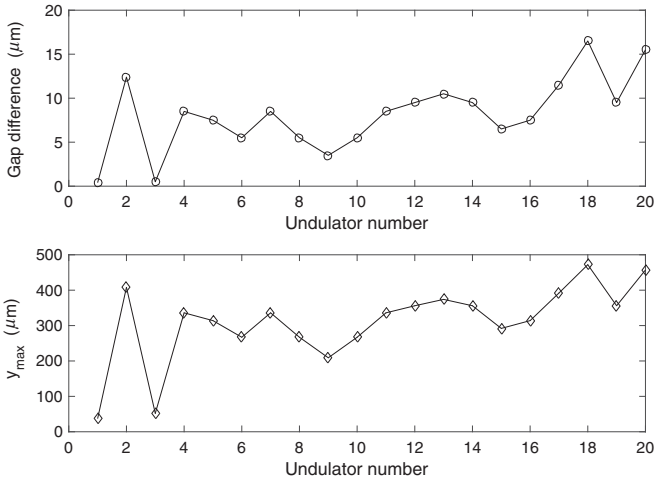

FIG. 12. Difference of undulator gap distances in Fig. 10 (top) and $y_{\max}$ of the tilt of the undulator segments (bottom).

A tilted undulator is schematically shown in Fig. 11. With the tilt parameterized as $y_{\max}$, the e-beam position y with respect to the undulator center can be represented as

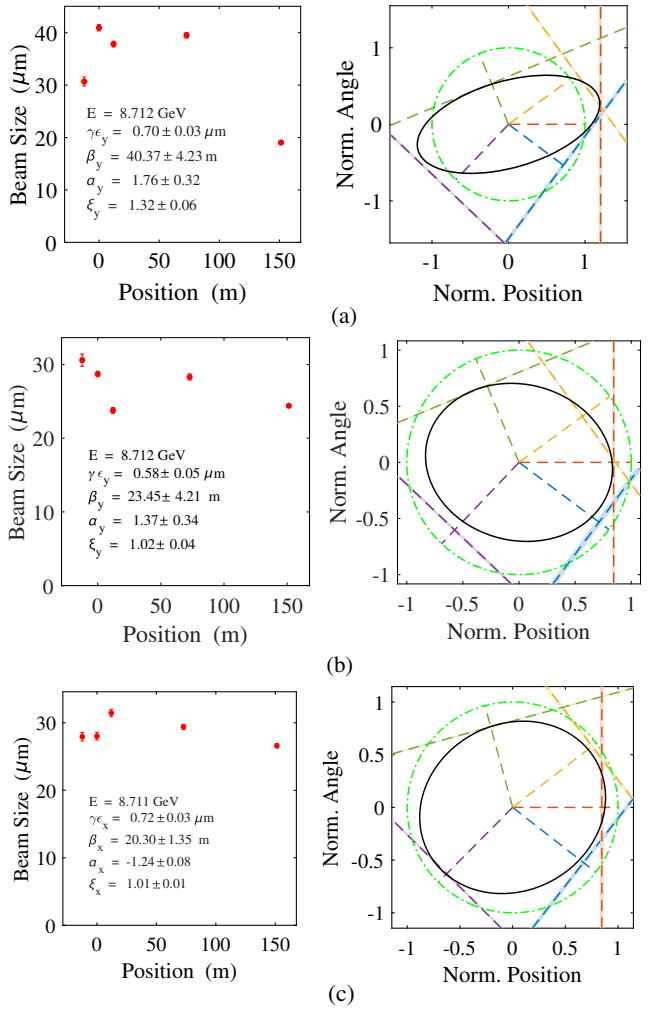

FIG. 13. Measurement of beam sizes and Twiss parameters using wire scanners in the undulator FODO lattice. Vertical beam sizes along the undulator line and the normalized phase space of the vertical plane (a) before matching and (b) after. (c) Horizontal beam sizes along the undulator line and normalized phase space of the horizontal plane after matching. The green circle in the phase space diagrams represents a phase space of a 1 mm mrad emittance beam. The horizontal axis of the beam size figures represents the relative distance along the undulator line with the second wire scanner located at position 0.

$$y(z) = \frac{y_{\max}}{L/2}\left(z - \frac{L}{2}\right), \tag{2}$$

where L is the undulator length (5 m).

We can calculate the undulator peak field change as a function of the gap distance change, $\Delta B = a\Delta g$, where Δg is the gap distance change determined by K tuning and a is a linear coefficient at a specific undulator K obtained from the undulator field measurement data. In order to have the same undulator K, the field integral amplitude should fulfill the following requirement:

$$B_0 L = \int (B_0 - \Delta B)\cosh(k_u y) dz, \quad (3)$$

where the left-hand part represents an initial field integral without the undulator tilt and the right represents the case in Fig. 11. For small ΔB, $y_{\max} = \frac{\sqrt{6a\Delta g/B_0}}{k_u}$. Figure 12 shows $y_{\max}$ of each undulator segment using the data of the undulator gap distance in Fig. 10. The highest value of $y_{\max}$ is 472 μm for HU18 in Fig. 12, which corresponds to a tilt angle of 189 μ rad. The tilt parameters $y_{\max}$ shown in Fig. 12 follow the trend of the ground movement; the places of HU02 and HU18 in the undulator hall show the steepest change of vertical position in time [14]. A tilt of an undulator segment subject to ground movement introduces an undulator field change visible to the electron beam, which can be corrected by the K tuning to accurately find the compensating gap distance.

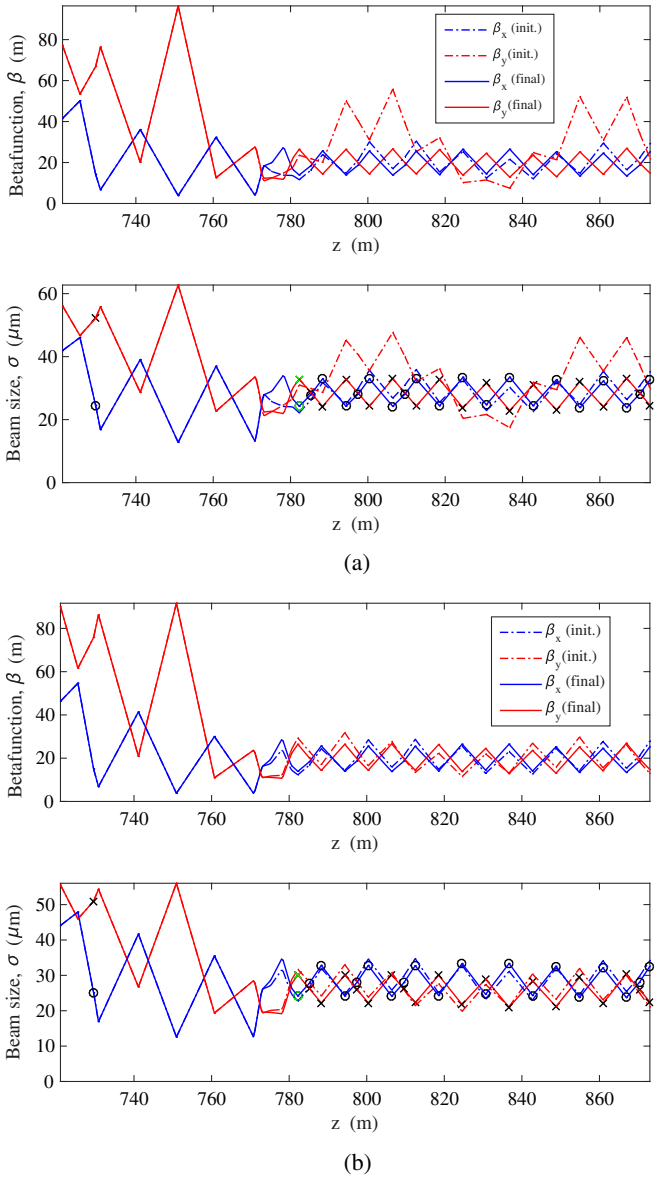

FIG. 14. Beta function and beam sizes along the undulator FODO lattice: (a) before and (b) after lattice matching. The dashed lines represent the measurements; the solid lines represent the expected functions after implementing the matching solution.

IV. LATTICE MATCHING

The lattice of the hard x-ray undulator line is 15 periods of FODO lattice, whose betatron phase advance is 40° per cell, with drift spaces between quadrupoles which can potentially accommodate 30 undulators, although only 20 undulators are currently installed. Five wire scanners are placed at the center of the drifts of the undulator line FODO lattice [15]. The locations of the wire scanners were selected among drift spaces (where undulators are not placed) in order to have more than 120° of accumulated betatron phase advance: three wire scanners upstream of the first undulator, one wire scanner at the self-seeding section in the middle of the undulator line, and one wire scanner right after the last undulator with phases of 0°, 40°, 80°, 160°, and 260°, respectively. The wire material is a 34-μm-thick carbon wire suitable for the undulator line, because it generates low-intensity radiation when it is hit by the electron beam. It takes 2 min to finish a one plane emittance measurement using five wire scanners, so it takes only 4 min for both planes. The five wire scanners are used for beam profile measurements at five different places to obtain emittance and Twiss parameters. By adjusting five quadrupoles located upstream of the FODO lattice, the measured Twiss parameters can then be matched to the design lattice.

This arrangement of wire scanners makes it possible to measure the exact size of the e beam interacting with the photon beam along the undulator line. Figure 13 shows the measurement of the beam size, emittance, and Twiss parameters using the wire scanners in the undulator FODO

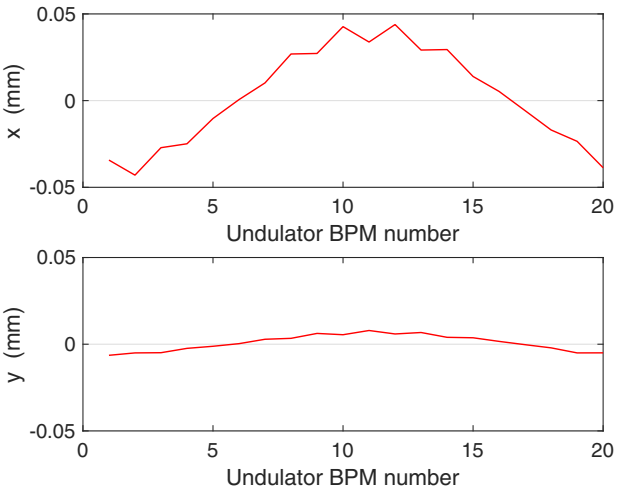

FIG. 15. One example of an orbit offset along the undulator line.

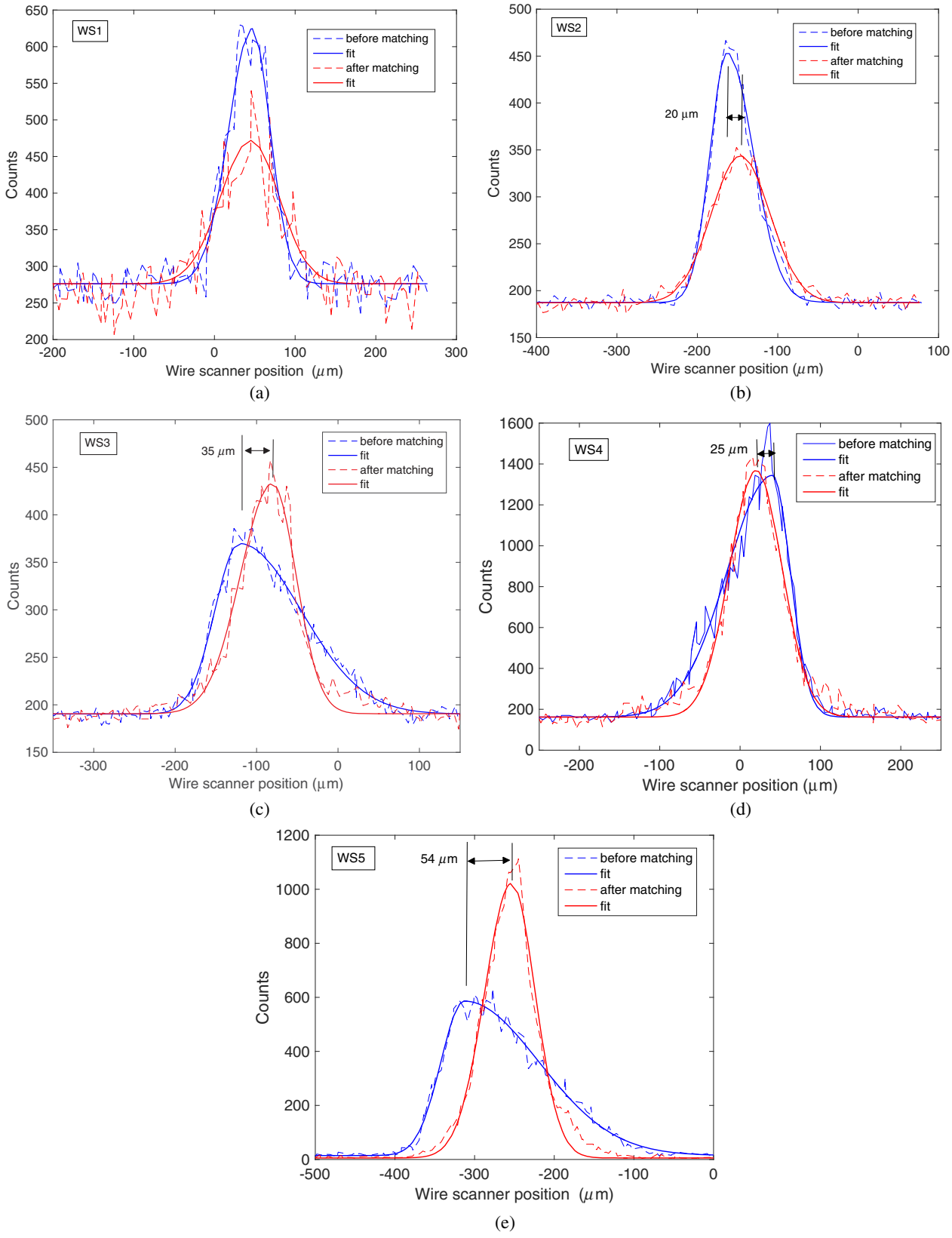

FIG. 16. Horizontal beam profiles measured by wire scanners at five different locations before and after the lattice matching: (a) WS1, (b) WS2, (c) WS3, (d) WS4, and (e) WS5. The distance marked in the figure represents the peak position shift of the electron beam distribution after the matching, while the position of the center of mass appears unchanged.

lattice. The right figure in Figs. 13(a)–13(c) represents the normalized phase space referenced to a 1 mm mrad emittance beam depicted by the green circle in the figure.

Figure 13(a) shows the measured Twiss parameters in the vertical plane before the lattice matching. The measured vertical emittance ($\gamma\epsilon_y$) is 0.70 mm mrad, and the mismatch parameter (ξ_y) is 1.32. The mismatch parameter in the figure, $\xi = \frac{1}{2}(\hat{\beta}\gamma - 2\alpha\hat{\alpha} + \beta\hat{\gamma})$, is defined as the difference between the measured Twiss parameters and the design lattice Twiss parameters, where α, β, and γ are the design Twiss parameters and $\hat{\alpha}$, $\hat{\beta}$, and $\hat{\gamma}$ are the measured Twiss parameters. The perfect matching case of $\alpha = \hat{\alpha}, \beta = \hat{\beta}$, and $\gamma = \hat{\gamma}$ corresponds to $\xi = 1$. It is clearly seen that the beam sizes are very different along the undulator line. After the matching, the emittance ($\gamma\epsilon_y$) is 0.58 mm mrad (vertical) in Fig. 13(b) and 0.72 mm mrad (horizontal) in Fig. 13(c). The mismatch parameter (ξ) of the measured Twiss parameters to the design FODO lattice is as small as 1.01 (horizontal) and 1.02 (vertical), and the beam sizes of both planes are almost uniform along the undulator line. Figure 14 shows the beta function and beam sizes along the undulator FODO lattice before and after the lattice matching. The beam sizes in both horizontal and vertical planes could be made uniform along the undulator line.

Using this emittance measurement and matching, the projected emittance has been maintained below 0.72 (horizontal) and 0.58 mm mrad (vertical) from the injector along the 700-m-long linac down to the undulator line. The same kind of wire scanner system is being used at L4 in Fig. 1. The measured emittances at L4 are 0.68 for the horizontal and 0.56 for the vertical plane. From Fig. 14(b), it is expected that optimizing the matching of the electron beam along the 100-m-long undulator line facilitates maximizing the overlap between the e beam and the photon beam.

After EBBA was successfully done as shown in Fig. 4, an FEL intensity over 800 μJ at 9.7 keV could be achieved. An orbit offset with respect to the EBBA reference orbit was necessary as shown in Fig. 15, which is one example of many different cases of intentional orbit offsets to increase the FEL intensity. However, this kind of orbit offset is not necessary after implementing lattice matching (the FEL intensity is also increased to 1.4 mJ).

Figure 16 shows the horizontal beam profile measured by wire scanners at five different positions before and after lattice matching. It is clearly seen that the asymmetrical profiles were improved to Gaussian ones after matching. A noteworthy observation is that there are some shifts of the peak intensity positions for all wire scanners due to matching, which may be a reason why a large horizontal orbit offset is necessary to increase the FEL intensity before matching is applied. Lattice matching with a wire-scanner-based Twiss parameter measurement along the undulator line allows one to make the e-beam distribution for optimum lasing coincide with the EBBA reference orbit, which makes it possible to maximize the spatial overlap between the electron and photon beam through the 100-m-long undulator line.

V. CONCLUSION

The hard XFEL tuning method combining EBBA with the undulator radiation spectrum analysis is conducive to generating a dispersion-free orbit, to finding the undulator field centers, and to determining the accurate value of the gap distance for the operating undulator K for each undulator segment, which proves to be highly reliable and robust for FEL lasing with variable-gap undulators.

The EBBA measurement with known vertical offsets of the undulators clearly shows a fit solution for the BPM and quadrupole offsets with an artificial bow pattern in the vertical plane. In order to avoid this effect from the natural focusing of the undulators, an initial EBBA should be performed with the undulator gap fully open. The tilt of an undulator segment subject to ground movement introduces an undulator field change visible to the e beam, which can be corrected with K tuning to accurately find a compensating gap distance. Lattice matching with a wire-scanner-based Twiss parameter measurement along the undulator line ensures that the EBBA reference orbit coincides with the e-beam distribution. Introducing an orbit offset along the undulator line for optimum FEL performance is not necessary after successfully implementing lattice matching.

The spatial overlap between the electron beam and photon beam can be maximized along the 100-m-long undulator line by using both EBBA and lattice matching. Furthermore, the spectral overlap of the undulator radiation from all undulators can be achieved through the undulator radiation spectrum analysis to accurately find the undulator K value and field center of each undulator, which are both affected by ground motion.

ACKNOWLEDGMENTS

This research is supported by the Ministry of Science and ICT of Korea [Grant No. 2018R1A6B4023605] and partly by the Basic Science Research Program [Grant No. 2017R1A2B4007274] through the National Research Foundation of Korea (NRF) funded by the Ministry of Science and ICT of Korea. The authors thank J. Loos for her valuable contributions to the beam studies and data analysis, and also the preparation of this manuscript.

APPENDIX: BEAM-BASED ALIGNMENT ALGORITHM

This Appendix summarizes the algorithm used for the EBBA procedure used at LCLS and PAL-XFEL based on Ref. [3]. A typical undulator FODO lattice is shown in Fig. 17 with an array of quadrupoles accompanied by adjacent beam position monitors and undulators located

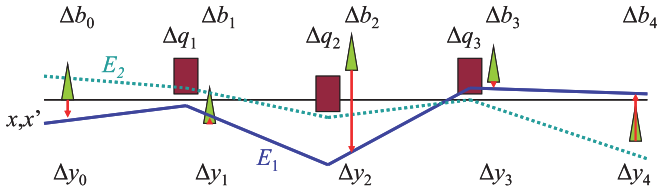

FIG. 17. Beam line configuration example for BBA. The green triangles depict BPM locations with absolute offsets Δb_i, and the dark red rectangles the quadrupoles with offsets Δq_i. Electron trajectories beginning at the left with launch offset x and angle x' are shown schematically for two energies $E_1 < E_2$. The observed beam positions Δy_i for each energy are shown as red arrows.

between the quadrupoles (not shown in the figure). Conventional alignment of a beam line will leave remaining positioning errors of quadrupoles and BPMs in the 50–100 μm range. The offset quadrupoles, remaining undulator field integrals, Earth's magnetic field, and other fields from surrounding structures will cause trajectory deviations to an even greater extent. If the beam is steered to the BPM centers, the mechanical BPM position accuracy is still more than an order of magnitude larger than the few-micrometer straightness requirement typically necessary for x-ray FEL operation.

The main goal of the BBA procedure is to determine the absolute offsets of the BPMs with micrometer accuracy and to find proper quadrupole offsets to compensate all the remaining dipole fields between quadrupoles, so that the beam can be steered to a dispersion-free straight line at the BPM locations. The trajectory straightness between BPMs and, particularly, along the undulators cannot be determined in this way and has to be inferred from undulator field measurements and simulations.

As an electron beam of infinite energy would travel on a straight line, the idea of the BBA algorithm is to measure the beam positions along the undulator beam line at several different beam energies while maintaining all magnetic fields within the undulator beam line the same. When extrapolating the measured beam positions to their values at infinite energy, they will represent the true BPM offsets. In practice, this is done by solving a system of equations relating the measured beam positions at different energies to the BPM and quadrupole offsets. The selected energy range for the measurement should be as large as possible, for the accelerator and the reciprocal energy values should be equally spaced to obtain linearly increasing focusing strengths for the undulator lattice.

Assuming no coupling terms in the beam transport matrices, the equations for the horizontal and vertical plane can be solved independently, and, hence, the subsequent discussion is for a single plane only. For BPM number j and beam energy E_k, the measured beam positions are denoted Δy_{jk}, the initial true launch position and angle x_k and x'_k (typically considered at the location of the first BPM of the undulator beam line), and the quadrupole and BPM offsets Δq_l and Δb_m. The system of equations can then be written as

$$\Delta y_{jk} = R^I_{jk} x_k + R^{I'}_{jk} x'_k + \sum_l R^Q_{jkl} \Delta q_l + \sum_m R^B_{jkm} \Delta b_m$$

with the launch response matrix

$$R^I_{jk} = R^{0\to \mathrm{BPM}_j}_{(1,1)}, \qquad R^{I'}_{jk} = R^{0\to \mathrm{BPM}_j}_{(1,2)}$$

denoting the (1,1) and (1,2) elements, respectively, of the transport matrix from the start of the undulator beam line to the location of the jth BPM evaluated at energy E_k, the quadrupole offset response matrix

$$R^Q_{jkl} = \begin{cases} R^{\mathrm{Q}_{l,\mathrm{End}}\to \mathrm{BPM}_j}_{(1,1)} - R^{\mathrm{Q}_{l,\mathrm{Begin}}\to \mathrm{BPM}_j}_{(1,1)} & \text{if } z(\mathrm{Q}_l) < z(\mathrm{BPM}_j), \\ 0 & \text{otherwise,} \end{cases}$$

and the BPM offset response matrix

$$R^B_{jkm} = -\delta_{jm}.$$

If the beam line consists of only BPMs, quadrupoles, and drift sections in between, i.e., an undulator beam line with retracted undulators, then it can be shown that any solution for the initial launch and BPM and quadrupole offsets is invariant to adding a linear function in beam line coordinate z to the offsets and initial launch conditions. This can be resolved by adding constraint equations for either the BPM or the quadrupole offsets to the system of equations; e.g., in the case of choosing BPM offsets, this can be stated as

$$0 = \sum_m \Delta b_m, \quad 0 = \sum_m z(\mathrm{BPM}_m) \Delta b_m,$$

which forces the BPM offsets to keep their average position and pointing. Alternatively, two columns in either the BPM or quadrupole offset response matrix, preferably located close to the start and end of the undulator line, can be removed to fix the offsets of the respective BPMs or quadrupoles to zero.

Further ambiguities can occur at the start and end of the undulator line from the placement of quadrupoles. A quadrupole nearby or upstream of the first BPM needs to be excluded, as the effect of its offset cannot be distinguished from the effect of a particular initial launch angle. Similarly, the offset of a quadrupole downstream or just before the last BPM under consideration also cannot be determined with sufficient accuracy.

In a practical application, the algorithm has to be used iteratively, as various effects will not permit a dispersion-free undulator orbit at the desired level of accuracy in one step. One iteration consists of acquiring beam orbits at several energies, fitting the offsets to the data, applying the BPM offset changes either by mechanical BPM movement or in

software, and correcting the beam orbit by either moving the quadrupoles by their offsets or using embedded steering correctors. Limitations in the acquisition step are due to BPM measurement noise, possible calibration errors in the BPM measurements, and nonlinear responses at large beam offsets which are particularly likely in the initial commissioning of an undulator beam line. During subsequent iterations of the algorithm, the effect of the systematic BPM errors will gradually diminish as the beam orbit becomes closer to a straight line. Errors in the application step of the procedure can result from the limited mechanical precision of BPM and quadrupole movers or calibration errors in the corrector steering coils. The effect of these errors will also become smaller during the BBA iterations. Once converged, the measured orbits will ideally be identical at all energies, limited only by BPM resolution and residual betatron oscillations from upstream beam jitter.

Poor or no conversion of the algorithm in the case of presumed large systematic errors in initial commissioning can be avoided by limiting the algorithm to correcting only the largest offsets and dipole field errors. This can be accomplished by using singular value decomposition as the fitting algorithm and applying corrections only based on the largest eigenvalues.

[1] H.-S. Kang *et al.*, PAL-XFEL technical design report, Pohang Accelerator Laboratory, 2014.

[2] H. Yang, G. Kim, and H.-S. Kang, First saturation of 14.5 keV free electron laser at PAL-XFEL, Nucl. Instrum. Methods Phys. Res., Sect. A **911**, 51 (2018).

[3] P. Emma, R. Carr, and H.-D. Nuhn, Beam-based alignment for the LCLS FEL undulator, Nucl. Instrum. Methods Phys. Res., Sect. A **429**, 407 (1999).

[4] H.-S. Kang *et al.*, Hard x-ray free-electron laser with femtosecond scale timing jitter, Nat. Photonics **11**, 708 (2017).

[5] T. Tanaka, S. Goto, T. Hara, T. Hatsui, H. Ohashi, K. Togawa, M. Yabashi, and H. Tanaka, Undulator commissioning by characterization of radiation in x-ray free electron lasers, Phys. Rev. ST Accel. Beams **15**, 110701 (2012).

[6] P. Emma *et al.*, First lasing and operation of an angstrom-wavelength free electron laser, Nat. Photonics **4**, 641 (2010).

[7] H. Tanaka *et al.*, A compact x-ray free-electron laser emitting in the sub-angstrom region, Nat. Photonics **6**, 540 (2012).

[8] C. Milne *et al.*, SwissFEL: The Swiss x-ray free electron laser, Appl. Sci. **7**, 720 (2017).

[9] H. Weise and W. Decking, Commissioning and first lasing of the European XFEL, in *Proceedings of the 2017 Free Electron Laser Conference*, Santa Fe, USA (JACoW, Geneva, 2017), pp. 9–13.

[10] T. O. Raubenheimer *et al.*, LCLS-II: Status of the cw x-ray FEL upgrade to the SLAC LCLS facility, in *Proceedings of the 2015 Free Electron Laser Conference, Daejeon, Korea* (JACoW, Geneva, 2015), pp. 618–624.

[11] H.-S. Kang *et al.*, Beam optics design for PAL-XFEL, in *Proceedings of the 2012 Free Electron Laser Conference, Nara, Japan* (JACoW, Geneva, 2012), pp. 309–312.

[12] J. Pflueger *et al.*, Status of the undulator system for the European x-ray free electron laser, in *Proceedings of the 2013 Free Electron Laser Conference* (JACoW, Geneva, 2013), pp. 367–371.

[13] S. Lee, Y. J. Park, C. Kim, S. H. Kim, D. C. Shin, J.-H. Han, and I. S. Ko, PAL-XFEL cavity beam position monitor pick-up design and beam test, Nucl. Instrum. Methods Phys. Res., Sect. A **827**, 107 (2016).

[14] H. J. Choi, S. B. Lee, H. G. Lee, S. Y. Back, S. H. Kim, and H. S. Kang, Wire position system to consistently measure, and record the location change of girders following ground changes, J. Phys. Conf. Ser. **874**, 012088 (2017).

[15] G. J. Kim *et al.*, Wire scanner measurement at the PAL-XFEL, in *Proceedings of the 2018 International Beam Instrumentation Conference, Shanghai, China* (JACoW, Geneva, 2018), pp. 445–447.